JOURNAL OF MATERIALS SCIENCE 26 (1991) 1545 - 1555

Strength characterization of MgO-partially stabilized zirconia

R. K. GOVILA
Material Systems Reliability Department, Scientific Research Laboratory, Ford Motor Company, P. O. Box 2053, Dearborn, MI 48121, USA

The flexural strength of MgO-partially stabilized zirconia was evaluated as a function of temperature (20–1300 °C in air environment), applied stress and time. The indentation-induced-flaw technique did not produce well-defined symmetrical cracks of controlled size, whose length (on the tensile surface) or depth (on the fracture face) can be measured unambiguously, and therefore it should not be used for measuring fracture toughness. The sudden decrease in fracture strength at moderately low temperatures (200–800 °C) is believed to be due to stability of the tetragonal phase and relative decrease in the extent of the stress-induced martensitic phase transformation of the tetragonal to monoclinic phase. Flexural stress rupture testing at 500–800 °C in air indicated the material's susceptibility to time-dependent failure, and outlines safe applied stress levels for a given temperature. Stress rupture testing at 1000 °C and above at low applied stress levels showed bending of specimens, indicating the onset of plasticity or viscous flow of the glassy phase and consequent degradation of material strength.

1. Introduction

Transformation-toughened zirconia ceramics represent a class of materials which possess high strength and toughness. The use of these materials for insulation and structural components (automotive) in adiabatic diesel engines [1–5] and other types of industrial applications [6–10] is being investigated. The primary reasons for their use in heat engine applications are low thermal conductivity (good insulation), high thermal expansion close to cast iron and steel, good oxidation and thermal shock resistance.

Pure zirconia (ZrO_2) melts at an extremely high temperature and shows three polymorphs, the monoclinic, tetragonal and cubic phases which undergo phase transformations as follows [7, 11]

$$\text{liquid} \xrightarrow{2680\,^\circ\text{C}} \text{Cubic} \xrightarrow{2370\,^\circ\text{C}} \text{tetragonal} \underset{1150\,^\circ\text{C}}{\overset{950\,^\circ\text{C}}{\rightleftharpoons}} \text{monoclinic} \quad (1)$$

The monoclinic phase is stable up to 1170 °C where it transforms to the tetragonal phase which is stable up to 2370 °C and the cubic phase exists up to the melting point of 2680 °C. Because of these phase transformations, pure zirconia cannot be used for high-temperature structural applications due to its inability to maintain structural integrity of a component subjected to heating and cooling cycles. However, certain cubic oxides such as MgO, CaO, Y_2O_3, CeO_2 and other rare-earth oxides stabilize the high-temperature cubic phase to room temperature and at the same time promote a decrease in the transformation temperatures. However, if insufficient stabilizing oxide is added than the amount required for full stabilization, a "partially stabilized zirconia" (PSZ) is formed. PSZ usually consists of two or more phases (cubic, tetragonal and monoclinic). The good mechanical properties of PSZ ceramics are primarily a result of stress-induced "martensitic" phase transformation of the metastable tetragonal phase to the stable monoclinic phase, hence the name "transformation toughening". In addition, selective thermal treatment (annealing at a given temperature in a specific phase field for a given time) further enhances the mechanical strength properties [12–19]. The MgO or CaO–PSZ consists of large-grained (40–65 μm) cubic zirconia matrix. Inside the cubic grains, a finely dispersed array of submicrometre size, ellipsoidal-shape tetragonal precipitates exists. Monoclinic zirconia is also present in these cubic grains and at the grain boundaries. The Y_2O_3 or CeO_2–PSZ can be controlled to contain almost 100% tetragonal zirconia phase. The grain size usually ranges from 1–5 μm and recently [20–22] submicrometre size has been achieved. These materials are often referred as "tetragonal zirconia polycrystal" or TZP.

In both types of PSZ (MgO- or Y_2O_3-doped), the tetragonal zirconia phase undergoes a stress-induced martensitic transformation to a monoclinic phase in the path of an advancing crack with an accompanying increase in volume of 3%–5% in the matrix and shear strain. This increase in volume produces compressive stresses surrounding the advancing crack and minor microcracking of the monoclinic phase. The compressive stresses tend to close the moving crack or crack opening and thereby increase resistance to crack

0022–2461/91 $03.00 + .12

propagation resulting in improved or high fracture toughness.

This study was undertaken to characterize the strength behaviour of a commercially available MgO–PSZ (TS grade) by evaluating fracture strength and toughness as a function of flaw size (pre-indented specimens) and temperature (20–1300 °C); failure sites and the mode of crack propagation were examined fractographically. In addition, long-term durability and reliability were characterized using flexural stress rupture testing at several temperatures.

2. Material, specimen preparation and testing

2.1. Material

The material used in this study was a commercial grade MgO–PSZ (Nilcra Ceramics Inc.) containing about 9 mol % MgO as stabilizer, designated TS grade, and overaged for improved thermal shock resistance. The material was obtained in the form of a cylinder (length 138 mm, inside and outside diameters 80 and 100 mm, respectively). Because the material's (TS grade) thermal and mechanical properties are well characterized by the manufacturer [23] and others [10, 19, 24–30], no X-ray diffraction studies were carried out in order to determine volume fractions of the cubic, tetragonal and monoclinic phases present in the as-machined test samples.

2.2. Specimen preparation and testing

Flexural test specimens (approximately 32 mm long × 6 mm wide × 3 mm thick) were machined from the cylinder (test component) wall. All faces were ground lengthwise using 320 grit diamond wheels; the edges were chamfered lengthwise to prevent notch effects. All specimens were tested in the as-machined condition and no further surface polishing or any heat treatment was carried out prior to testing.

For flexural strength evaluation, specimens were tested in one-quarter-point, four-point bending (inner span is one-half of the outer span) in an Instron testing machine (Model 1125) using a specially designed self-aligning ceramic fixture [31] made from hot-pressed SiC. The outer and inner knife edges of the testing fixture were spaced approximately 19 and 9.5 mm apart, respectively. The high-temperature bend tests were conducted in air using a rapid temperature-response furnace attached to the testing machine head. In high-temperature tests, specimens were held at the test temperature for 15 min to achieve thermal equilibrium before testing was begun. No preload was applied on test specimens for either room-temperature or high-temperature tests. All specimens were tested at a machine crosshead speed (MCS) of 0.5 mm min^{-1}.

The flexural stress rupture tests at elevated temperatures (400–800 °C) in air environment were also conducted in four-point bending using the self-aligning ceramic fixture and furnace. The load was applied to the test specimen through a lever-arm, dead-weight-type assembly. The experimental set-up was equipped with a microswitch to cut off power to the furnace and the timer at the instant specimen failure occurred. The total time to failure was recorded. Complete details regarding the design and operation of the stress-rupture test rig are given elsewhere [32].

2.3. Indentation-induced flaw technique

Test specimens used in this technique were identical to those used for flexural strength evaluation except that these were pre-indented using the Vickers diamond pyramid microhardness indentor (Wilson Instrument Division, ACCO) and tested in a similar fashion to the previous specimens. Indenting the MgO–PSZ (TS grade) with a Vickers indentor did not result in the introduction of well-defined and symmetrical surface cracks as observed in many ceramic and brittle materials earlier [33–37]. It should be pointed out that among those specimens which were pre-indented and subsequently tested in four-point bending, some failed at the pre-indented (precracked) site and some failed at other sites. This behaviour was observed throughout the temperature range of investigation and with varying indentation loads (10–30 kg) as shown later. A schematic representation of crack geometry in a test specimen and details of the indentation-induced flaw technique have been reviewed earlier [33–40]. All preindentation (precracking) was done at room temperature on as-machined surfaces of flexural test specimens.

3. Results and discussion

3.1. Microhardness indentation

The use of the microhardness indentation-induced flaw (IIF) technique [33–40] in producing reproducible surface cracks in many ceramic materials whose geometry (shape, close to semicircular) and size (depth of crack) are controlled by choice of indentor load, is well established. This method has been used successfully in hot-pressed and sintered silicon nitrides [34–36, 41], sintered SiC [42], and lithium–aluminium–silicate glass-ceramic [43] to show that these ceramic materials closely approximated the Griffith criterion for brittle fracture. In addition, this method allowed the determination of fracture energy or toughness and estimation of the approximate flaw size in as-machined uncracked test specimens. Therefore, a series of as-machined specimens was prepared and pre-indented with microhardness indentation loads ranging from 10 kg (~ 98 N), 20 kg (~ 196 N) and 30 kg (~ 294 N) in order to determine the fracture strength as a function of flaw (crack) depth. Upon subsequent testing in flexure, it was found that many specimens did not fail at the pre-indented site but failed in close proximity to or away from it, Fig. 1c. A typical example of a Vickers microhardness indentation made on the polished surface of a specimen using 10 and 20 kg indentation load is seen in Fig. 1. Note that the indentation does not produce well-defined and symmetrical surface cracks, and therefore, test specimens are less likely to fail at the indentation site. It should be pointed out that among those specimens which failed at the indentation site, the crack front on

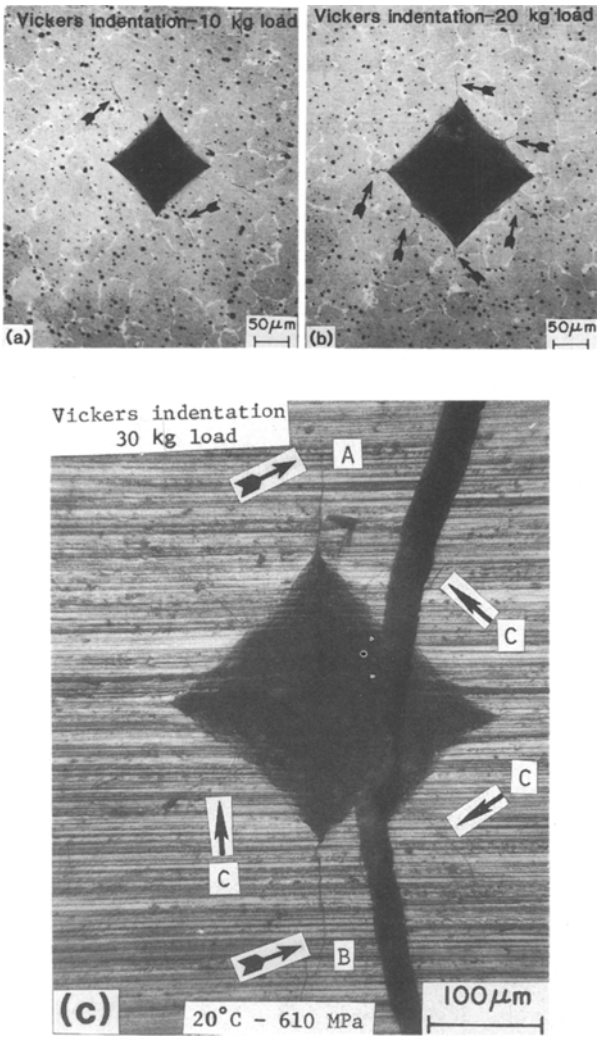

Figure 1 Optical micrographs showing Vickers microhardness indentations on (a, b) polished and (c) as-machined surfaces of MgO–PSZ (TS grade) specimens. The microstructure showing large cubic grains, uniform distribution of fine porosity (black dots, 2%–4%) and delineation of grain-boundaries due to eutectoid decomposition on cooling is clearly visible. Vickers indentations did not produce controlled, symmetrical and reproducible cracks. Specimen shown in (c) did not fail at the pre-indented site and the crack AB was not present at the time indentation was made, but developed or nucleated during testing of the specimen. Arrows marked C show nucleation of random cracks surrounding the indentation.

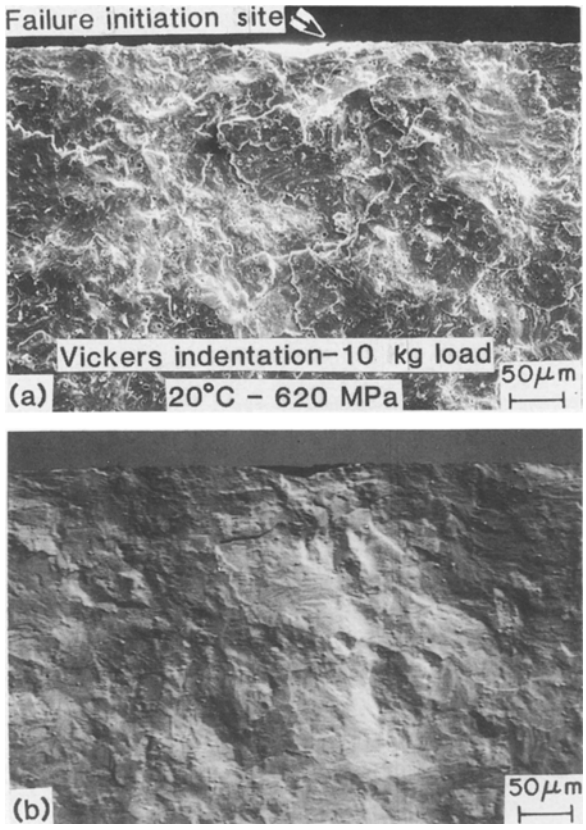

Figure 2 Scanning electron micrographs showing fracture surface of a specimen in which failure initiation occurred at the pre-indentation site. (a) Crack front is not visible. (b) Same area as seen in (a), fractograph taken in back-scattered mode to reveal the surface structure. Crack front is still not visible.

the fracture face was not visible and crack depth could not be measured, Fig. 2. Previous studies [35, 41–43] in other ceramic materials have clearly shown the importance of high-temperature testing in revealing the size and shape (semi-circular or semi-elliptical) of the precracked (pre-indented) region possibly due to residual stress relief and subsequent stable crack propagation (sub-critical crack growth). Therefore, several pre-indented specimens were tested at higher temperatures (600–1200 °C) and showed similar behaviour to that observed at 20 °C as shown in Fig. 3, for a specimen tested at 1000 °C. Furthermore, specimens containing indentations with significantly large and varying indentation loads (10–30 kg) did not show a significant variation in fracture strength (σ_F) and the magnitude of σ_F was comparable to that observed in as-machined (unindented or uncracked) specimens (see Table I). Using single-edge notch beam method, the fracture toughness of MgO–PSZ (TS grade) at 20 °C as reported by the manufacturer [18] is about 8 MPa $m^{1/2}$ and the Vickers diamond indentation method gives a slightly higher value.

Recently, Becher and Ferber [29] investigated the strength properties of MgO–PSZ (TS grade) using the IIF technique, and were able to introduce significantly long surface cracks (~ 400 μm) using a 9.1 kg (~ 89 N) indentation load. In addition, on subsequently testing these pre-indented specimens in flexure at temperatures of 22, 500 and 1000 °C with failures occurring at the indentation site, Becher and Ferber [29] were able to measure the total surface flaw lengths of 600, 500 and 440 μm, respectively. Unfortunately, Becher and Ferber [29] did not present either surface micrographs of the pre-indentation region showing nucleation of well-defined cracks, or corresponding fracture surfaces, to demonstrate that the semi-circular region can be identified and the resulting crack depth can be measured accurately. Therefore, the reason for the discrepancy observed between the present study and that reported by Becher and Ferber [29] for the same material is not clear.

The fact that large initial indentations made on the as-machined surfaces of specimens did not produce well-defined cracks deep enough to degrade the material's fracture strength clearly points out the high toughness of this material (MgO–PSZ, TS grade) in comparison to other ceramic materials like alumina,

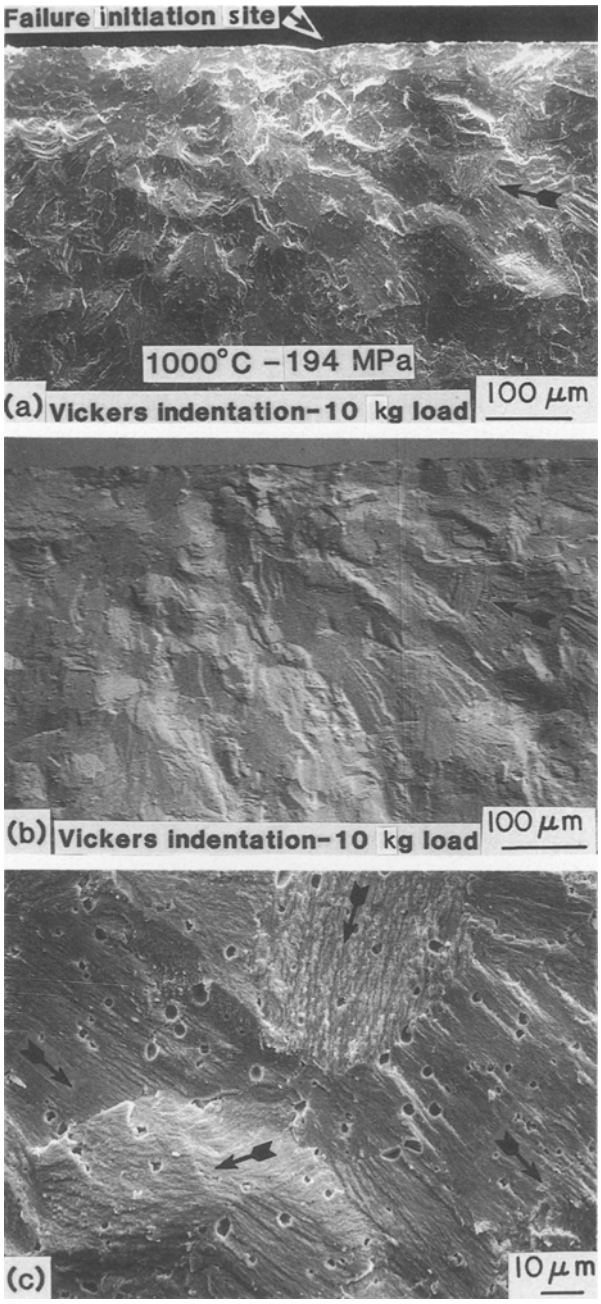

Figure 3 Scanning electron micrographs showing fracture surface of a specimen in which failure occurred at the pre-indentation site. (a) In spite of testing at a high temperature, the crack front is not visible. (b) Same area as seen in (a) but in back-scattered mode and the crack depth cannot be determined. (c) Arrows indicate the direction of crack propagation from grain to grain.

silicon nitride and silicon carbide. In short, it has been shown in this study that the IIF technique cannot be used for determining the fracture energy or fracture toughness, either at 20 °C or at elevated temperatures. Similar observations have been made by Schioler [44] in evaluating MgO–PSZ.

3.2. Flexural strength versus Temperature

At room temperature (20 °C), a total of ten specimens were tested in four-point bending to determine the fast fracture strength. A typical statistical variation in fracture strength, σ_F, at 20 °C is shown in Fig. 4. The σ_F varied from a minimum of 641 MPa to a maximum

TABLE I Fast fracture strength data for MgO–PSZ (TS grade)

Test no.	Test temp. (°C)	Fracture strength (MPa)	Failure origin
1	20	675	Surface flaw
2		685	Surface flaw
3		664	Surface flaw
4		675	Surface flaw
5		670	Surface flaw
6		713	Surface flaw
7		675	Surface flaw
8		716	Surface flaw
9		641	Surface flaw
10		659	Surface flaw
11	200	676	Surface flaw
12		664	Surface flaw
13		564	Corner failure
14		659	Surface flaw
15		650	Surface flaw
16	300	612	Surface flaw
17		609	Surface flaw
18		510	Surface flaw
19		483	Surface flaw
20		604	Surface flaw
21	400	483	Surface flaw
22		516	Corner failure
23		554	Surface flaw
24		538	Surface flaw
25		543	Surface flaw
26	500	384	Surface flaw
27		450	Surface flaw
28		461	Surface flaw
29		417	Surface flaw
30		445	Surface flaw
31	600	384	Surface flaw, Fig. 7.
32		373	Corner failure
33		380	Surface flaw
34		375	Surface flaw
35		347	Surface flaw
36	800	406	Surface flaw
37		417	Surface flaw
38		359	Surface flaw
39		389	Surface flaw
40		415	Surface flaw
41		445	Surface flaw
42	1000	342	Surface flaw
43		318	Surface flaw
44		351	Surface flaw
45		376	Surface flaw
46		334	Surface flaw
47	1200	171	Surface flaw, Fig. 8
48		198	Surface flaw
49	1300	165	Subsurface flaw, Fig. 9
Pre-indented specimens, Vickers indentation load 10 kg			
50	20	653	Did not fail at the indentation site
51		620	Failed at the indentation site, Fig. 2
52	600	307	Did not fail at the indentation site
53	1000	194	Failed at the indentation site, Fig. 3
54	1200	228	Did not fail at the indentation site
55	1200	162	Did not fail at the indentation site
Pre-indented specimens, Vickers indentation load 20 kg			
56	20	582	Failed at the indentation site
57		604	Failed at the indentation site
Pre-indented specimens, Vickers indentation load 30 kg			
58	20	610	Did not fail at the indentation site Fig. 1c
59	20	582	Failed at the indentation site

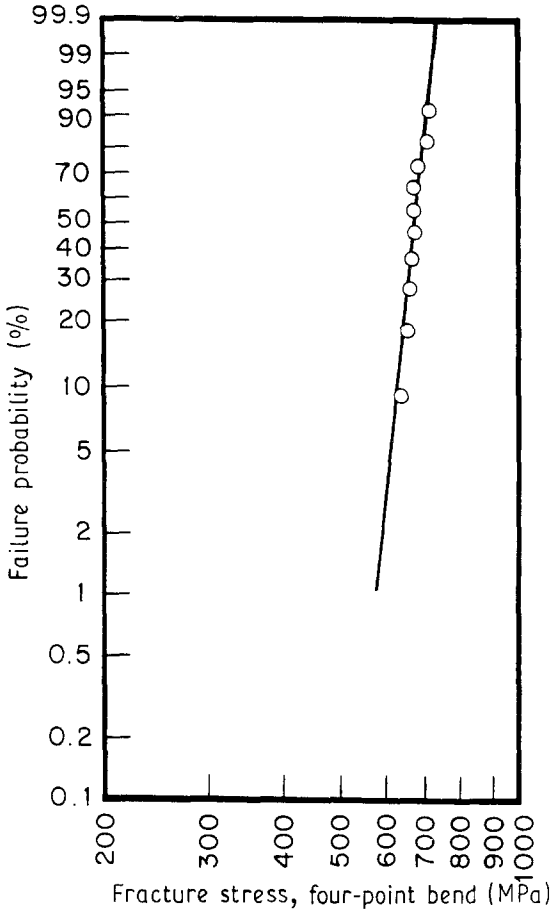

Figure 4 Statistical variation in fracture strength for polycrystalline MgO–PSZ (TS grade), at 20 °C. σ_{ave} = 677 MPa, S. D. 32 Mpa, m = 26.

of 716 MPa with an average strength of 677 MPa, Weibull modulus of 26, and a standard deviation of 32 MPa. These values are in agreement with the manufacturer's data [23]. Most of the ceramic materials usually show low Weibull modulus values ranging from 5 to 12, indicating large scatter in materials strength due to variations in flaw sizes. The high value of Weibull modulus (26) obtained from test specimens cut out from an engine component is a strong measure of excellent uniformity in composition, processing and fabrication. However, it is possible that this high value of Weibull modulus could be due to the small number of samples tested. It should be pointed out that the load–deflection curves for specimens tested at 20 °C displayed non-linear (deviation from the elastic line) behaviour possibly due to stress-induced transformation of the tetragonal phase to monoclinic phase during testing and disappeared at higher temperatures as discussed later. Examination of the fracture surfaces in all specimens tested at 20 °C suggested surface-initiated failures related to grain-boundary cracking. The identification and location of failure origin was found to be extremely difficult possibly due to large cubic grain size. However, occasionally failure-initiating sites associated with processing contaminants or powder impurities were observed as shown in Fig. 5. Failure-initiating regions varied in size, ranging from 100–115 μm long, along the tensile edge of the fracture surface and 70–80 μm deep. Detailed examination of the failure origin, Fig. 5b, revealed the presence of oxide inclusions of aluminium and silicon. It is

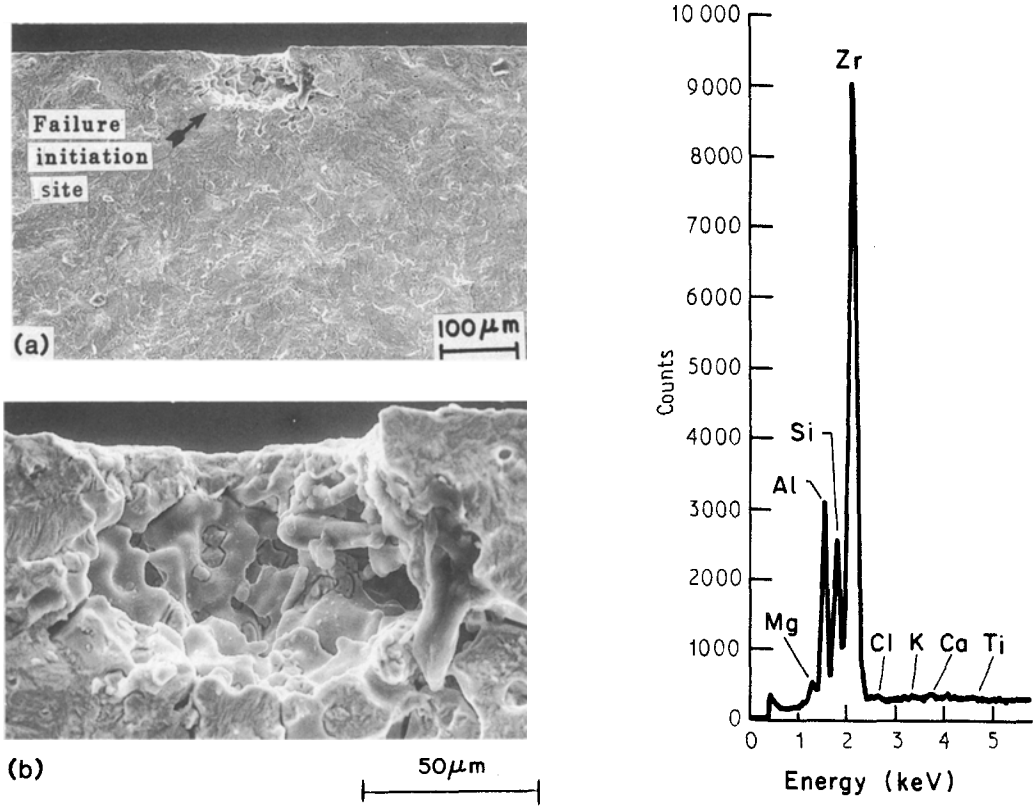

Figure 5 Scanning electron micrographs showing failure initiation occurring at a surface initiated flaw in MgO–PSZ (TS grade) specimen tested at 20 °C in a fast fracture mode (MCS = 0.5 mm min^{-1}). (b) Note the occurrence of melted or glassy phase material inside the failure region. Energy-dispersive X-ray spectra taken inside the failure region revealed the presence of aluminium and silicon.

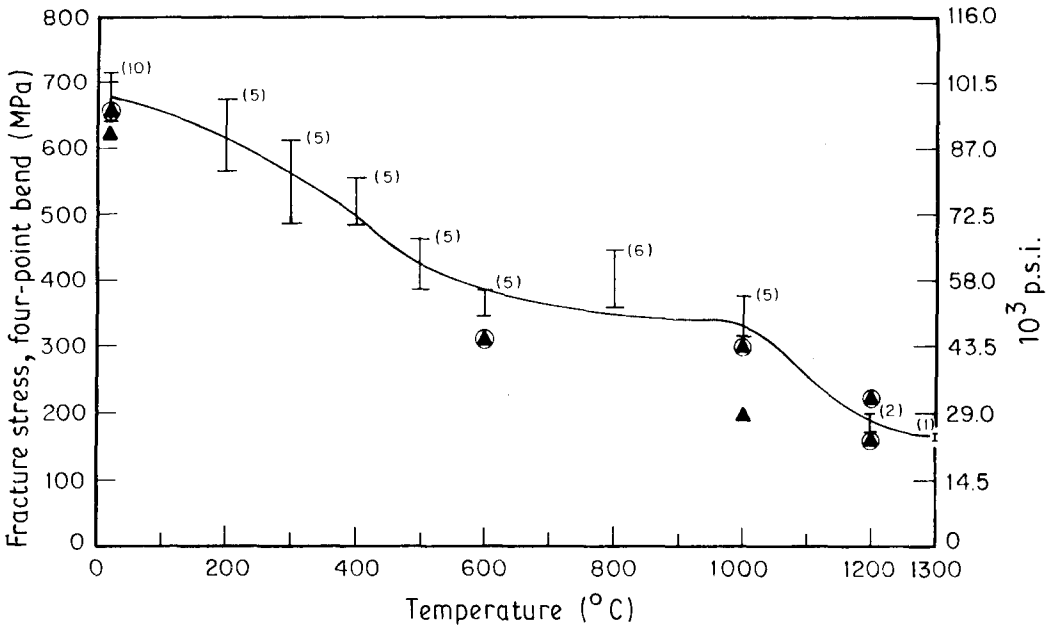

Figure 6 Variation in fast fracture strength of MgO–PSZ as a function of temperature. All specimens were tested at a MCS = 0.5 mm min^{-1}. (▲) Specimens with 10 kg Vicker's indentation; (◬) did not fail at the indentation site. Complete strength data are given in Table I.

believed that aluminium may have been introduced as a contaminant during ball milling of the powder using alumina balls and silicon is associated with small amounts of silica (SiO_2) present as an impurity in the powder. The presence of SiO_2 is beneficial in producing improved densification of the ceramic via liquid-phase sintering and detrimental in degrading the mechanical strength both at 20 °C and higher temperatures, due to its presence as a grain-boundary glassy phase. Recently, Drennan and Hannink [45] have pointed out the benefits of small additions of strontia (SrO) to MgO–zirconia alloys in reducing the deleterious effects of SiO_2. However, in the majority of test specimens, examination along the tensile edge of the fractured specimen showed intergranular cracking as shown later. From the fractographs, it appears that the primary mode of crack propagation during fast fracture (catastrophic failure) was primarily intergranular, and sometimes a mixed mode of fracture consisting of intergranular and transgranular crack growth. It appears that MgO–PSZ (TS grade) can be fabricated to large components, and the flexural strength can be improved by optimizing the sintering additives and conditions, and minimizing the presence of oxide inclusions.

Flexural strength was also evaluated at higher temperatures (200–1300 °C) and the variation in σ_F as a function of temperature is shown in Fig. 6. The decreasing σ_F with increasing temperature is clearly visible in Fig. 6. Pre-indented specimens showed similar behaviour. It is believed that the decrease in fracture strength at temperatures as low as 300 °C is due to increased stability of the tetragonal phase and decreased extent of the stress-induced martensitic phase transformation of the tetragonal phase to

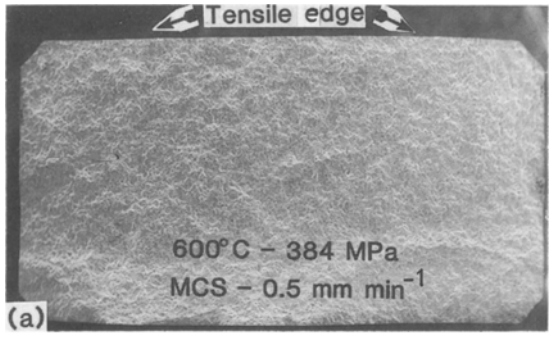

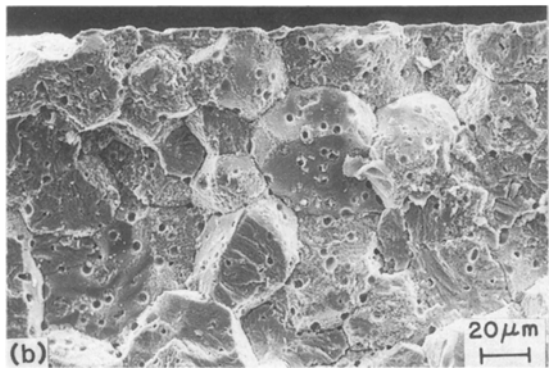

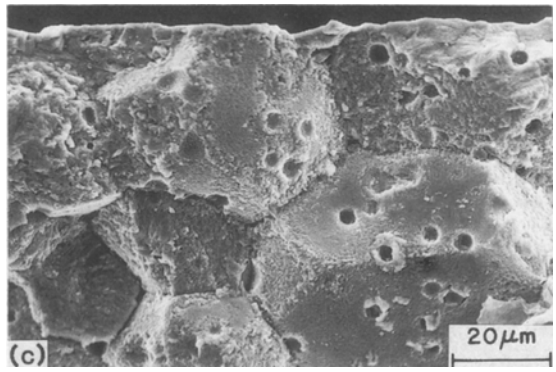

Figure 7 Typical fracture surface as seen in SEM. (a) Overall view of the fracture surface. (b) Localized group of cubic grains showing intergranular cracking and possibly the failure origin. (c) Grain-boundary cracking and opening.

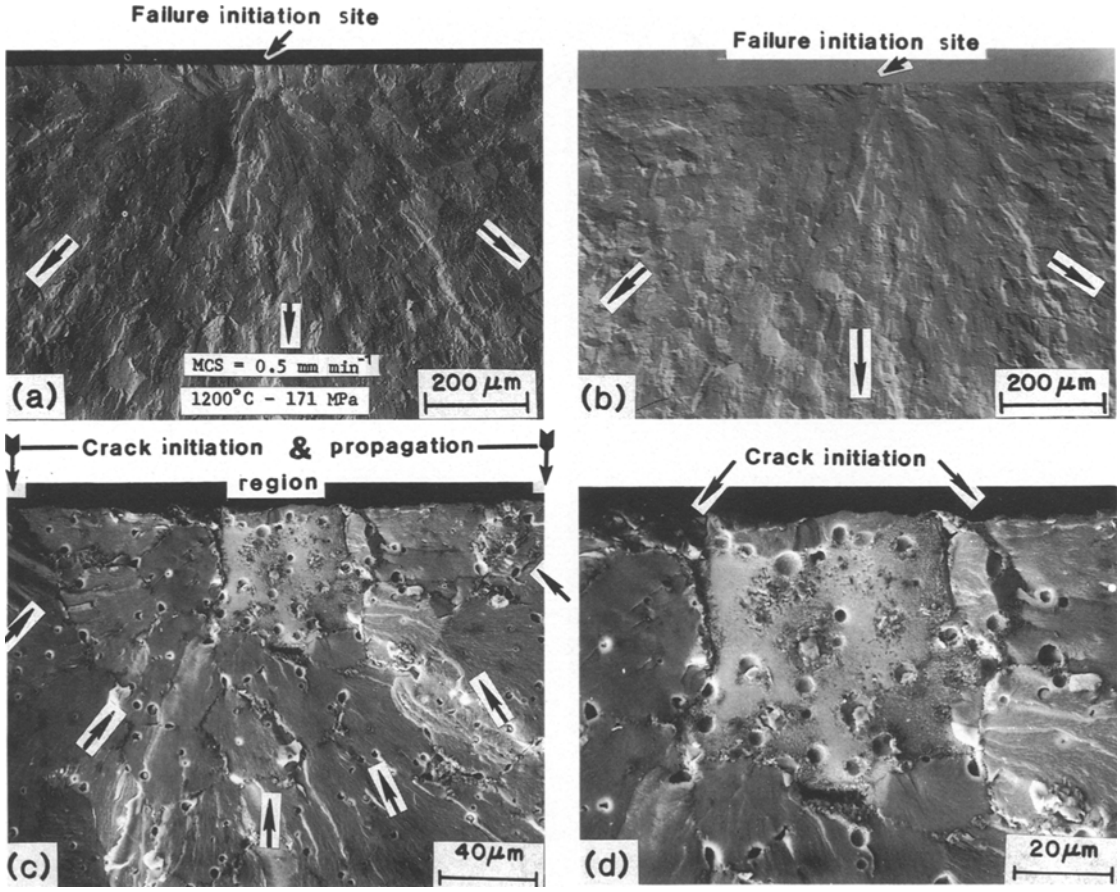

Figure 8 Typical example of a surface initiated failure as seen in SEM. (a) Fracture surface. (b) Same area as seen in (a) but fractograph taken in a back-scattered mode indicating the location of failure-initiation site. Arrows indicate the direction of crack propagation. (c) Higher-magnification view of the failure-initiation site showing crack initiation and propagation region. Arrows outline approximately the boundary of the effective flaw resulting in catastrophic failure. (d) Higher magnification view showing crack initiation site and the associated grain-boundary sliding.

monoclinic phase. This behaviour increases with increasing temperature, hence the decreased fracture strength and toughness. The sudden decrease in σ_F from 20 °C (average = 677 MPa) to 600 °C (average σ_F = 372 MPa, see Table I) is not encouraging in regard to use at moderately applied stress levels for long-term applications in diesel engine components, as discussed in the next section. In spite of the decreased fracture strength at elevated temperatures (200–1200 °C), the identification of the fracture origin was difficult and the fracture surfaces were similar in appearance to those observed at 20 °C as typically seen in a specimen failed at 600 °C, Fig. 7. Fractographic examination along the tensile edge showed a localized region where intergranular cracking along several cubic grains was visible, Fig. 7b, c. The uniformly distributed fine porosity, ranging in size from 2–4 μm and approximately circular in shape as seen on the polished surface, Fig. 1a, b, and on the fracture face, Fig. 7c, did not seem to promote the initiation of fracture directly. Although, the presence of pores along the grain boundaries would weaken the bond strength between grains, no failure sites associated with a porous region were observed in any specimen tested either in fast fracture mode (Fig. 6) or stress rupture mode, as discussed later.

The σ_F appears to be constant in the temperature region 600–1000 °C. The fracture surfaces were similar in their appearance up to 1000 °C (see Figs 2, 3 and 7) and did not show significant grain-boundary decomposition products as observed at 1200 and 1300 °C. A sudden and sharp drop in σ_F was noticed in tests made at 1200 °C and above, σ_F decreased to almost one-quarter of the room temperature strength (Fig. 6). Typical fracture surfaces for specimens tested in a fast fracture mode at 1200 and 1300 °C are shown in Figs 8 and 9, respectively. The fracture surface at 1200 °C, Fig. 8, is a typical example of a surface-initiated type flaw commonly seen in MgO–PSZ at all temperatures (20–1300 °C), Table I. It should be noted that the topographic features of the fracture surface seen in back-scattered mode, Fig. 8b, clearly delineate the location of failure initiation. Examination of the failure site distinctly reveals grain-boundary cracking associated with multiple cubic grains, Fig. 8c, and possibly suggests a semicircular zone as a final flaw size prior to catastrophic failure, as indicated by arrows. It appears that the failure initiated intergranularly in the large cubic grain, Fig. 8d, propagated to other grains intergranularly under stress and achieved a critical flaw size resulting in catastrophic failure. Evidence of transgranular cleavage is clearly visible, Fig. 8c. At 1300 °C, the failure initiation site appears to be subsurface, Fig. 9a, and this becomes distinctly clear when examined in the back-scattered mode, Fig. 9b. Detailed examination of the failure initiation

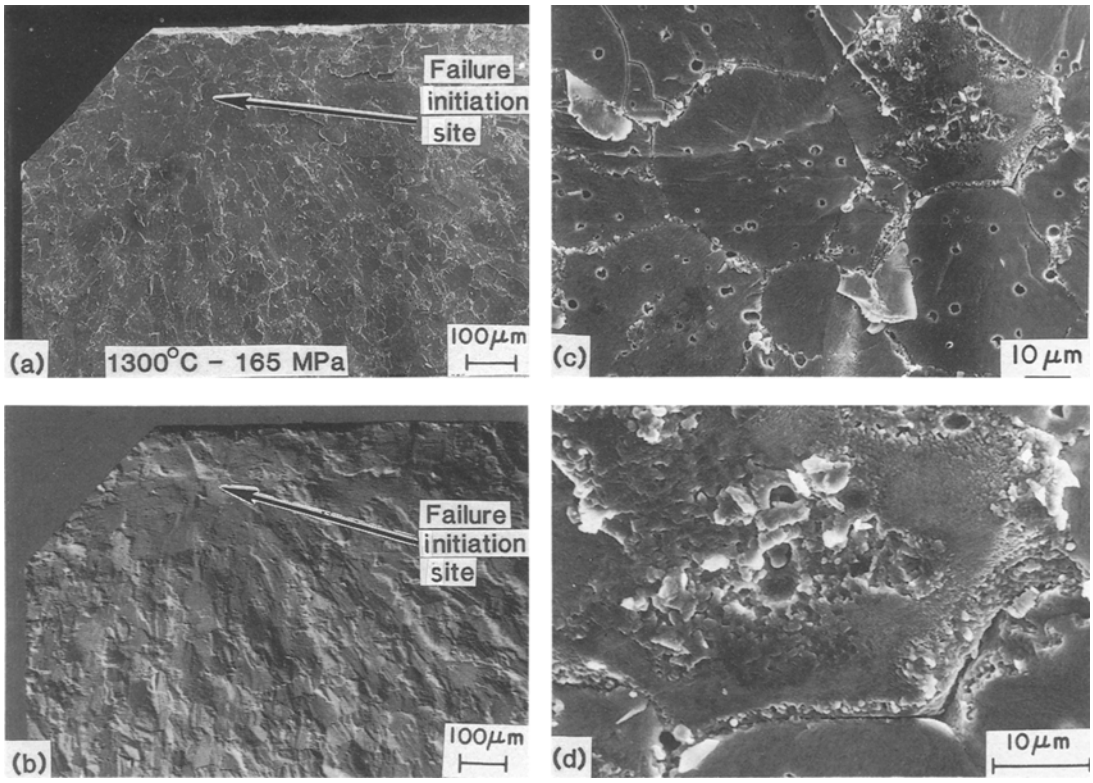

Figure 9 SEM fractographs showing failure occurring at a subsurface site. (a) Fracture surface. (b) Same area as seen in (a) but in a back-scattered mode to reveal the surface structure. Note the smooth region surrounding the failure-initiation site and the river-line type markings radiating from it clearly identify the location of failure origin. (c) Higher magnification view of the failure site showing intergranular cracking associated with multiple cubic grains. Transgranular cleavage is also visible. (d) Higher magnification view showing eutectoid decomposition products inside the cubic grain and along the grain-boundaries.

site did not reveal the presence of any oxide inclusions of Al, Si and Fe, but showed intergranular cracking along several cubic grains, Fig. 9c, and significant decomposition product along the grain boundaries was noticed, Fig. 9d. The fracture origin did not show any signs of plastic deformation and the cubic grains displayed signs of cleavage fracture, Fig. 9c. The load–deflection curve at 1300 °C for this specimen (Fig. 9) showed completely linear elastic behaviour indicating the absence of creep deformation. Up to 1300 °C, the fractured specimens (Fig. 9) did not show any signs of bending, thus confirming the absence of plastic and creep deformation during fast fracture testing (machine crosshead speed = 0.5 mm min^{-1}). Even though, the above observations strongly discount the presence of significant viscous flow of the glassy phase resulting in slow (subcritical) crack growth, the sudden decreased fracture strength at elevated temperatures, 1000–1300 °C, was probably partly due to limited creep deformation as confirmed in stress rupture tests at 1000 °C and above.

3.3. Flexural stress rupture

Previous studies [35, 41, 43, 46, 47] have clearly shown that majority of the high-strength ceramic materials are susceptible to strength degradation at low or intermediate temperatures due to static oxidation and stress-enhanced oxidation, stress corrosion cracking due to the presence of moisture, and at high temperatures ($\geqslant$ 1000 °C) due to sub-critical crack growth and oxidation as well. Therefore, flexural stress rupture tests were carried out as a function of temperature (400–800 °C) and applied stress in order to determine (a) the material's susceptibility for intermediate temperature instability, (b) the presence of slow (subcritical) crack growth (SCG) at 400–800 °C, and (c) to identify allowable stress levels for a limited time ($\leqslant$ 500 h). A total of 39 specimens was tested in the stress rupture mode and the results are summarized in Table II.

At 400 °C, two specimens sustained the applied stress of 344 MPa for 240 and 332 h, respectively, without showing failure and bending. As the applied stress was increased to 413 MPa, failure occurred in 169 h. Examination of the fracture surface in SEM did not reveal the failure initiation site.

At 500 °C, three specimens sustained the applied stress of 276 MPa for 500 h without showing failure and bending. As the applied stress was increased to 344 MPa, five specimens out of six failed in 1, 6 min, 1, 4.6 and 258 h, and the sixth sustained the stress for 315 h without showing failure and bending. Fractographic examination of the fracture surfaces of all five specimens failed to reveal the failure initiation site.

At 600 °C and 276 MPa, five specimens were tested. One specimen failed in short duration (0.11 h) while the other four specimens sustained the applied stress for 163, 310, 332 and 510 h, respectively, and did not show any bending. As the applied stress was increased

TABLE II Flexural stress rupture results for MgO–PSZ (TS grade)

Test no.	Test temp. (°C)	Applied stress (MPa)	Failure time (h)	Sustained time without failure (h)	Discoloration, specimen bending and fracture origin
1	400	344	–	240	Off-white, no bending
2		344	–	332	Off-white, no bending
3		413	169	–	Off-white, no bending, failure site not visible
4	500	276	–	500	Off-white, no bending
5		276	–	525	Off-white, no bending
6		276	–	577	Off-white, no bending
7		344	0.017	–	Off-white, no bending, failure site not visible
8		344	0.10	–	Off-white, no bending, failure site not visible
9		344	1.0	–	Off-white, no bending, failure site not visible
10		344	4.6	–	Off-white, no bending, failure site not visible
11		344	258	–	Off-white, no bending, failure site not visible
12		344	–	315	Off-white, no bending
13	600	276	0.11	–	Off-white, no bending, failure site not visible
14		276	–	163	Off-white, no bending
15		276	–	310	Off-white, no bending
16		276	–	332	Off-white, no bending
17		276	–	546	Off-white, no bending
18		310	0.25	–	Off-white, no bending, failure site not visible
19		310	–	240	Off-white, no bending
20		310	–	312	Off-white, no bending
21		344	0	–	Failed instantly, failure site not visible
22		344	0.017	–	Off-white, no bending, failure site not visible
23		344	0.034	–	Off-white, no bending, failure site not visible
24		344	0.10	–	Off-white, no bending, failure site not visible
25		344	0.20	–	Off-white, no bending, failure site not visible
26		344	–	239	Off-white, no bending
27		344	–	258	Off-white, no bending
28	800	276	120	–	Off-white, no bending, iron inclusion, Fig. 10
29		276	–	386	Off-white, no bending
30		310	0.10	–	Off-white, no bending, failure site not visible
31		310	–	237	Off-white, no bending
32		310	–	240	Off-white, no bending
33		344	0	–	Failed instantly, failure site not visible
34		344	12	–	Off-white, no bending, grain-boundary cracking
35		344	39	–	Off-white, no bending, grain-boundary cracking
36		344	163	–	Off-white, no bending, grain-boundary cracking
37	1000	207	–	90	Off-white, specimen showed bending at 20 h, Fig. 11
38	1100	138	–	90	Off-white, specimen showed bending at 20 h, Fig. 11
39	1200	138	–	20	Off-white, specimen showed bending at 20 h, Fig. 11. Applied stress was increased to 276 MPa, specimen failed instantly and fracture surface showed grain-boundary cracking

As-processed material was white in colour.

to 344 MPa, the time-to-failure decreased significantly as displayed by five specimens failing between 0 (instant) and 0.2 h (see Table II), and two specimens sustained the stress for over 200 h without showing failure and bending.

At 800 °C and 276 MPa, two specimens were tested. One specimen sustained the stress for 386 h without showing failure and bending, while the other specimen failed in 120 h. Examination of the fracture surface in the scanning electron microscope (SEM) revealed that the failure occurred at a surface-initiated inclusion, Fig. 10, consisting of iron contamination, possibly picked up during processing. As the applied stress was increased to 344 MPa, four specimens were tested and all failed in 0 (instant), 12, 39 and 163 h, respectively. Examination of the fracture surfaces in SEM failed to reveal the initiation and identification of the failure origin.

At 1000 °C and above, specimens subjected to low applied stress levels such as 207 MPa for short durations like 20 h showed bending, indicating the onset of plastic and creep deformation, Fig. 11 (see Table II). It should be noted that these tests point out the importance of stress rupture testing in showing a material's instability (bending) at temperatures of 1000 °C and above, compared to fast fracture testing at similar temperatures which failed to detect the onset of plasticity or creep deformation.

In short, it is clear from the flexural stress rupture results that the material (MgO–PSZ, TS-grade) is incapable of sustaining applied stress levels of 344 MPa at temperatures of 500 °C and above. In

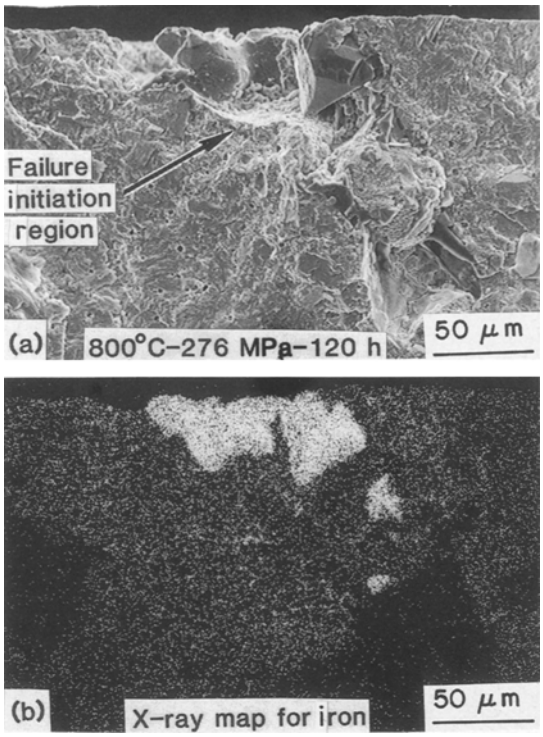

Figure 10 SEM fractographs showing failure initiation at an iron inclusion.

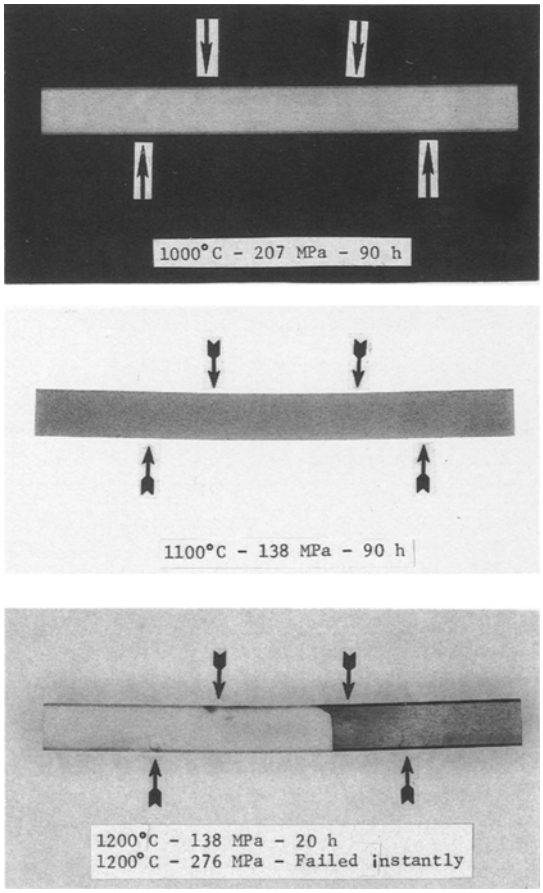

Figure 11 Overall view of the flexural specimens tested in stress rupture mode at elevated temperatures showing bending (creep deformation). The black coloration seen on the specimen tested at 1200 °C was due to carbon coating in order to examine the fracture face in SEM. The fracture surface was similar in appearance to that seen at 1300 °C (Fig. 9) except increased eutectoid decomposition was noticed. Arrows indicate approximate positions of inner and outer loading edges.

addition, occasional failures occurring at temperatures of 600 and 800 °C at a low applied stress level of 276 MPa clearly point out the material's susceptibility for failure possibly due to machining damage and processing contaminants.

4. Conclusion

The indentation-induced flaw technique did not produce well-defined and symmetrical surface cracks on the tensile surface of as-machined test samples. In addition, fracture surfaces of those specimens which failed in flexure testing at the pre-indentation site did not reveal the shape and size (depth) of the crack front. Therefore, the IIF technique should not be used for measuring fracture energy or toughness of MgO–PSZ (TS-grade).

Flexural strength decreased significantly with increasing temperature and this effect was noticeable at temperatures as low as 500 to 600 °C. Failure occurred in a brittle manner and the mode of crack propagation during fast fracture was a mixture of intergranular and transgranular crack growth.

Extensive flexural stress rupture evaluation in the temperature range 500–800 °C has identified the stress levels for time-dependent and time-independent failures. In addition, stress rupture testing at 1000 °C and above clearly revealed the onset of plastic deformation or viscous flow of the glassy phase and consequent degradation of the material strength.

Acknowledgements

The author thanks D. Cassidy, G. DeBell, W. Trela and L. Swank, for discussions, and R. Allor for providing micrographs used in Fig. 5, Dr Peter Beardmore for reviewing the paper, Y. T. Lu, R. Goss and Dr W. T. Donlon for SEM work (see Table I).

References

1. W. BRYZIK and R. KAMO, "Tacom/Cummins Adiabatic Engine Program", 1983 International Congress and Exposition, SAE Paper 830314, Detroit, MI, February 1983.
2. M. MARMACH, D. SERVENT, R. H. J. HANNINK, M. J. MURRAY and M. V. SWAIN, "Toughened PSZ Ceramics – Their Role as Advanced Engine Components", *ibid.*, paper 830318.
3. M. E. WOODS, W. F. MANDLER Jr and T. L. SCOFIELD, *Ceram. Bull.* **64** (1985) 287.
4. *Idem, ibid*, **64** (1985) 292.
5. D. W. RICHERSON, *ibid.* **64** (1985) 282.
6. R. H. J. HANNINK, M. MARMACH, M. J. MURRAY and M. V. SWAIN, See Table I.
7. R. STEVENS, "An Introduction to Zirconia", Magnesium Elektron Ltd, June 1983.
8. E. M. LOGOTHETIS, "Zirconia Oxygen Sensors in Automotive Applications", "Advances in Ceramics", Vol. 3, "Science and Technology of Zirconia", edited by A. H. Heuer and L. W. Hobbs (American Ceramic Society, Columbus, Ohio, 1981) p. 388.
9. R. C. GARVIE, C. URBANI, D. R. KENNEDY and J. C. MCNEUER, *J. Mater. Sci.* **19** (1984) 3224.
10. N. CLAUSSEN, M. RUHLE and A. H. HEUER (eds), "Advances in Ceramics", Vol. 12, "Science and Technology of Zirconia" (American Ceramic Society, Columbus, OH, 1984).

11. M. RUHLE and A. H. HEUER, "Phase Transformations in ZrO_2-Containing Ceramics: II, The Martensitic Reaction in t-ZrO_2", *ibid.* pp. 14–32.
12. D. L. PORTER and A. H. HEUER, *J. Amer. Ceram. Soc.* **60** (1977) 183.
13. D. L. PORTER, A. G. EVANS and A. H. HEUER, *Acta Metall.* **27** (1979) 1649.
14. F. F. LANGE, *J. Mater. Sci.* **17** (1982) 225.
15. *Idem, ibid.* **17** (1982) 235.
16. *Idem, ibid.* **17** (1982) 240.
17. *Idem, ibid.* **17** (1982) 247.
18. *Idem, ibid.* **17** (1982) 255.
19. R. H. J. HANNINK and M. V. SWAIN, *J. Aust. Ceram. Soc.* **18** (1982) 53.
20. I. ODA, M. MATSUI and T. SOMA, "Strength and Durability of PSZ Ceramics", paper presented at the International Symposium on Ceramic Components for Engine, Hakone, Japan, October 1983.
21. K. TSUKUMA, Y. KUBOTA and T. TSUKIDATE, "Thermal and Mechanical Properties of Y_2O_3-Stabilized TZP", in "Advances in Ceramics", Vol. 12, "Science and Technology of Zirconia", edited by N. Claussen, M. Ruhle and A. H. Heuer (American Ceramic Society, Columbus, OH, 1984) pp. 382–90.
22. M. MATSUI, T. SOMA and I. ODA, *J. Amer. Ceram. Soc.* **69** (1986) 198.
23. NILCRA CERAMICS, INC., Elmhurst, IL, USA, Product Update Brochure (1985).
24. R. H. J. HANNINK and R. C. GARVIE, *J. Mater. Sci.* **17** (1982) 2637.
25. R. H. J. HANNINK, *ibid.* **18** (1983) 457.
26. D. B. MARSHALL, *J. Amer. Ceram. Soc.* **69** (1986) 173.
27. A. G. EVANS and R. M. CANNON, *Acta Metall.* **34** (1986) 761.
28. P. F. BECHER, *J. Mater. Sci.* **21** (1986) 297.
29. P. F. BECHER and M. K. FERBER, *ibid.* **22** (1987) 973.
30. A. H. HEUER, *J. Amer. Ceram. Soc.* **70** (1987) 689.
31. R. K. GOVILA, Technical Report TR 80-18 (Army Materials and Mechanics Research Center, Watertown, MA, 1980).
32. R. K. GOVILA, J. A. HERMAN and N. ARNON, "Stress Rupture Test Rig Design for Evaluating Ceramic Material Specimens", Paper No. 85-GT-181, ASME Gas Turbine Meeting, 18–21 March, 1985, Houston, Texas.
33. R. K. GOVILA, *Acta Metall.* **20** (1972) 447.
34. J. J. PETROVIC, L. A. JACOBSON, P. K. TALTY and A. K. VASUDEVAN, *J. Amer. Ceram. Soc.* **58** (1975) 113.
35. R. K. GOVILA, K. R. KINSMAN and P. BEARDMORE, *J. Mater. Sci.* **14** (1979) 1095.
36. R. K. GOVILA, *J. Amer. Ceram. Soc.* **63** (1980) 319.
37. R. K. GOVILA, P. BEARDMORE and K. R. KINSMAN, "Strength Characterization and Nature of Crack Propagation in Ceramic Materials", in "Fractography and Materials Science", ASTM STP 733, edited by L. N. Gilbertson and R. D. Zipp (American Society for Testing and Materials, Philadelphia, PA, 1981) pp. 225–45.
38. B. R. LAWN, A. G. EVANS and D. B. MARSHALL, *J. Amer. Ceram. Soc.* **63** (1980) 574.
39. G. R. ANSTIS, P. CHANTIKUL, B. R. LAWN and D. B. MARSHALL, *ibid.* **64** (1981) 533.
40. P. CHANTIKUL, G. R. ANSTIS, B. R. LAWN and D. B. MARSHALL, *ibid.* **64** (1981) 539.
41. R. K. GOVILA, *J. Mater. Sci.* **23** (1988) 1141.
42. *Idem, ibid.* **19** (1984) 2111.
43. R. K. GOVILA, K. R. KINSMAN and P. BEARDMORE, *ibid.* **13** (1978) 2081.
44. L. J. SCHIOLER, "Effect of Time and Temperature on Transformation Toughened Zirconias", Technical Report TR 87-29, US Army Materials Technology Laboratory, Watertown, MA, June 1987.
45. J. DRENNAN and R. H. J. HANNINK, *J. Amer. Ceram. Soc.* **69** (1986) 541.
46. R. K. GOVILA, J. A. MANGELS and J. R. BAER, *ibid.* **68** (1985) 413.
47. R. K. GOVILA, *Am. Ceram. Soc. Bull.* **65** (1986) 1287.

Received 5 September 1989
and accepted 19 February 1990